Measurements of *G-H* and *H-I* fine-structure intervals in $n=7$, 9, and 10 helium Rydberg states

G. D. Stevens and S. R. Lundeen
Department of Physics, Colorado State University, Fort Collins, Colorado 80523
(Received 10 May 1999)

We have made measurements of the $7G$-H, $7H$-I, $9G$-H, $9H$-I, and the $10G$-H intervals in helium. These measurements are in good agreement with theoretical calculations up to the level of about 1 kHz precision. This confirms the importance of retardation to the intervals with about 1% precision. At the 1 kHz level, however, systematic discrepancies are seen which cannot be accounted for by suggested additional retardation corrections. [S1050-2947(99)00912-9]

PACS number(s): 32.30.Bv, 31.30.Jv

I. INTRODUCTION

Recent progress in both experimental and theoretical studies of the fine structure of Rydberg states of helium has been motivated largely by the suggestion that this system could be used to test predictions of certain long-range ''retardation'' forces between the Rydberg electron and the He^+ ion core [1]. In the extreme long-range limit ($r \gg 137a_0$) these forces are proportional to $\hbar/c$, where $\hbar$ is Planck's constant and c is the speed of light, so they are clearly nonclassical in nature. As a result of this progress, the leading effects of retardation on helium fine structure are now well understood theoretically and have been confirmed by experiment. Unfortunately, the connection with long-range forces has remained elusive since it has not yet been possible to measure the fine structure of Rydberg states whose binding energies directly reflect the simple long-range force first suggested by Spruch *et al.* [1,2]. Most of the precise measurements to date have been confined to the $n=10$ level of helium, where fine-structure intervals connecting states ranging from $L=2$ to 8 have been reported [3–5]. While the agreement with theoretical calculations is quite good by any objective standard (agreement to five or six figures in the fine-structure intervals), there are some small but significant discrepancies with the best calculations that are not yet understood. The order of magnitude of these discrepancies in $n=10$ (around 1 kHz) is comparable to certain additional ''retardation corrections'' which have been suggested [6,7], but inclusion of these suggested corrections fails to bring the theory and experiment into agreement. As additional tests of these calculations, we report here measurements of G-H and H-I fine-structure intervals in $n=7$ and 9 levels of helium, and a remeasurement of the $10G$-H interval.

II. EXPERIMENTAL TECHNIQUE

Our measurements, like other recent helium fine-structure measurements, were carried out using a fast atomic beam and a form of microwave/optical spectroscopy, which we refer to as RESIS (resonant excitation Stark ionization spectroscopy). The primary improvements over previous work were as follows.

(i) The use of a cesium vapor, rather than Ar gas, in the charge exchange cell [8]. This increased the fractional population of the $n=7$, 9, and 10 levels.

(ii) Improved design of the Rydberg detector, incorporating an electrostatic lens to improve collection efficiency after ionization.

(iii) Extension of the CO_2 laser detection to include $n=7$ and 9 levels as described below.

Items (i) and (ii) led to an improved S/N by about a factor of 15 over previous studies. This was very helpful, both in reducing the total time needed for the measurements and in allowing for more complete checks of systematic effects.

Our RESIS apparatus (see Fig. 1) starts with a beam of fast, ~10 kV helium ions that is incident on a cesium vapor charge-exchange cell. The helium ions capture an electron from the cesium atoms, forming a fast neutral beam with a substantial population of Rydberg states. The resulting beam then passes through two sets of field plates which Stark-ionize high-n Rydberg states, and deflect ions out of the neutral beam. The high-n, Stark-ionizable (detectable) states would otherwise produce an unwanted background signal.

Transitions between the lower Rydberg states and the upper, Stark-detectable Rydberg states are driven optically using Doppler-tuned CO_2 lasers. Since we are working with a fast beam with $v=0.0022c$, where c is the speed of light, we can Doppler-tune nearly continuously between the discrete molecular transitions in the CO_2 laser spectrum. The $n=9$ and 10 states are excited in a single step to detectable levels (9–20 or 10–30). The laser excitation of $n=7$ states to detectable levels requires two steps. A $^{13}CO_2$ laser is used to excite $n=7-9$ transitions, and then a conventional $^{12}CO_2$ laser continues the excitation from $n=9-20$.

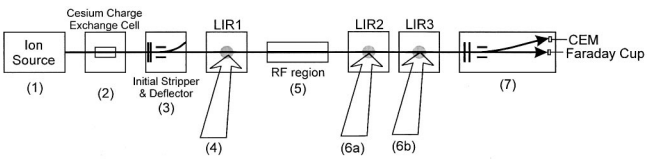

FIG. 1. Experimental block diagram of components used in the RESIS technique. A Colutron accelerator creates a helium ion beam at (1). This beam is neutralized in a cesium charge exchange cell (2). The remaining ion beam is deflected and upper Rydberg states are field-ionized at (3). CO_2 laser beams interact with the fast Rydberg beam in the laser interaction regions (LIR's) at (4), (6a), and (6b). rf transitions are driven in (5) (see Fig. 2 for a cross section of the transmission line). Signal atoms are Stark-ionized and detected at (7).

TABLE I. Laser excitation schemes used for specific rf transitions. Stark diagnostic peaks are listed where applicable.

	LIR	$7G$-H	$7H$-I	$9G$-H	$9H$-I	$10G$-H
prepare:	LIR 1	$7H$-$9I$	$7H$-$9I$	$9H$-$20I$	$9H$-$20I$	$10H$-$30I$
detect:	LIR 2	$7H$-$9I$	$7I$-$9K$	$9H$-$20I$	$9H$-$20I$	$10G$-$30H$
detect:	LIR 3	$9I$-$17K$	$9K$-$17L$			
diagnostic:		$17\ ^1F$-^1G	$17\ ^1F$-^1G	$20G$-H	$20G$-H	$17\ ^1F$-^1G

The five rf transitions studied in this experiment are listed in Table I, along with the specific laser transitions used to detect one of the states of the rf transition. In order to insure a population difference between the two states, an initial laser interaction (LIR 1) is used to deplete the population of one of the states prior to the rf interaction, as is indicated in Table I. Also shown in Table I are the high-n helium transitions that were monitored as diagnostics of stray electric fields within the rf region.

Transitions between specific fine-structure states in a given n level are driven in an rf transmission line. If the rf frequency is resonant with the transition, it causes a change in the population of the detected level which leads to a change in the detected ion current. The rf field is generated by a microwave synthesizer, and is 100% amplitude modulated at a frequency of about 2 kHz. Using a phase-sensitive lock-in amplifier with this reference frequency, we synchronously detect changes in the final ion current created by rf transitions.

The rf region used for the majority of the measurements in this paper was an off-axis 50 Ω transmission line. A cross section of the region geometry is included in Fig. 2. The $7G$-H spectra were taken using a short, rectangular cross-section waveguide (similar to that used in previous work [9]) that was designed for higher frequencies.

A number of measures were taken in order to insure that our measurements were not heavily perturbed by stray fields. First, the entire rf region was encased in mu-metal in order to reduce the earth's magnetic field. Due to the speed of our helium beam, any stray magnetic fields create motional electric fields that in turn induce Stark shifts in our measurements. Using a gauss meter we checked that our shielding kept magnetic fields below an rms value of 5 mG within the interior of the rf region.

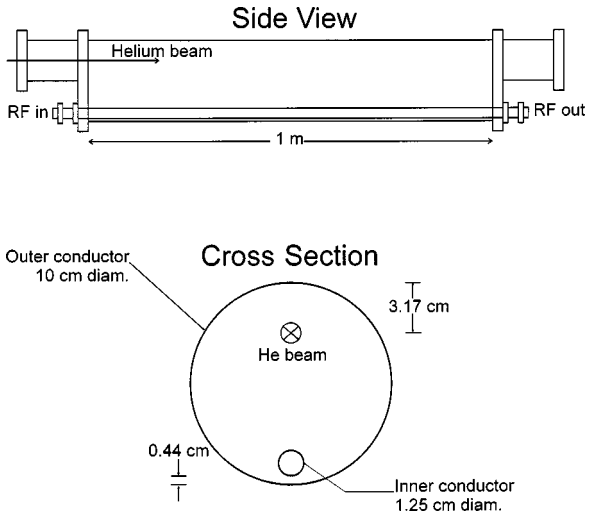

FIG. 2. Cross section of off-axis rf transmission line.

We used high-n diagnostic transitions that have large Stark shift rates as sensitive electric-field probes in order to measure the remaining electric fields within our rf regions. Using these diagnostic lines, we noticed that heating the rectangular rf region reduced and stabilized the electric fields present. We thus implemented a closed-circuit hot-oil heating assembly to heat the region uniformly and maintain a temperature of 90 °C during our $7G$-H measurement. Our other measurements were taken using the circular rf region, and heating this region did not reduce the observed electric fields. No heat was applied during data acquisition using this region.

Our first set of $10G$-H measurements was taken with stray electric fields of about 12 mV/cm in the rf region. For the second set of $10G$-H measurements, we placed a fixed bias voltage on the center conductor. This procedure is discussed in Sec. V, and it effectively reduced the size of the electric fields in the region by a factor of 2.

After passing through the rf region, the atoms enter a second laser interaction region, which transfers some of the population from the states of interest to detectable higher-n ($n=17$, 20, or 30) states. These signal atoms are then Stark-ionized in our detector. The detector makes use of several different longitudinal field regions in order to ionize the high-n Rydberg levels and tag the signal ions with an energy that is higher than that of the background ion beam. These energy-tagged signal ions are spatially separated from the background ions by use of an applied transverse electric field and drift region, which deflects the two ion beams by different amounts. The signal ions are collected and their current multiplied by a channel electron multiplier. Changes in this current synchronous with modulation of the rf amplitude constitute the measured rf signal.

As an example of a specific excitation scheme used in the experiment, consider the $9G$-H measurement outlined in Table I. The neutral fast Rydberg beam enters the initial stripper where population is removed from the $n=20$ states but not from the lower $n=9$ states. LIR 1 is set on the $9H$-$20I$ optical transition, which drives population out of the $9H$ state, thereby creating a population difference between the $9G$ and $9H$ states. Next, transitions are driven between these two states in the rf region, resulting in an increase in the population of the $9H$ state. This population is then detected by excitation of the $9H$-$20I$ optical transition, followed by Stark-ionization of the $n=20$ state. In this manner, we sensitively detect transitions driven between the $9G$ and $9H$ states.

The rf spectra show a fully resolved four-peak structure, with each resonance peak corresponding to a transition between corresponding levels of the fourfold magnetic fine structure of each level, as illustrated in Fig. 3. Figures 4, 5, and 6 illustrate the observed spectra.

III. MEASUREMENTS

A typical set of raw data for a given transition consisted of careful measurement of the signal for both directions of rf propagation (copropagating and counterpropagating). Elimination of the Doppler shifts is complicated by small reflections from the end of the rf region, which result in a weak traveling wave moving opposite to the main field. These reflections distort the line shape and could introduce errors in the line center if the two ends of the rf region reflect differently. For this reason, data were also taken with the rf region physically reversed half-way through each measurement, in order to interchange the two ends and the corresponding reflections. The two resulting copropagating and the two counterpropagating sets of data were averaged together to create two sets of data that each exhibit an average of the reflections from both ends of the region. These two sets of data were then fit as described below in Sec. IV, to extract the line centers of the four transitions ν_1, ν_2, ν_3, and ν_4.

Complete sets of data were taken for two separate beam velocities for each measured interval. For the $7G$-H, $7H$-I, $9G$-H, and $9H$-I intervals, accelerating potentials of 7 and 9 kV were used. For the $10G$-H intervals, we chose to make measurements at 8 and 9 kV. Taking data at two separate velocities provides a check as to whether our treatment of rf reflections and other line-shape altering effects is adequate. The position of the reflection peaks is linear in $\beta=v/c$, and the underlying reflection structure thus has a strong dependence on the beam velocity. The observed good agreement between the fits for two independent velocities indicates that our theoretical fit line shape (see Sec. IV) is complete enough to eliminate shifts in the line-center frequencies due to rf reflections.

Data were acquired daily by scanning repeatedly over the desired frequency range in uniform steps of 0.1 MHz (or 0.2 MHz for the $7G$-H data) for both directions of rf propagation with respect to the beam. Data were taken for 3 or 4 days for a given interval, and then the rf region was reversed. After completing the measurements with the rf region reversed, we switched beam velocities and repeated the full set of measurements. A typical interval measurement has about 40 h of cumulative data-acquisition time.

In order to extract values for the mean fine-structure (MFS) intervals, the intervals between the statistically weighted mean energies of the four nL states, we measured each of the four allowed transitions between MFS components, $\nu_1-\nu_4$ and also two additional weak transitions, ν_a and ν_b. These additional transitions (see caption of Fig. 3 for notation) were used to extract the lower state triplet separation with the relation

$$\nu({}^3L_{L-1}-{}^3L_{L+1})=\nu_a+\nu_b-\nu_1-\nu_2. \tag{1}$$

Because the transitions corresponding to ν_a and ν_b are only weakly allowed, much higher rf powers were required to observe them, leading to relatively large ac Stark shifts in these transitions. Consequently, these two transitions were measured at varying rf powers, and then extrapolated to zero power to remove the effects of ac Stark shifts. Using the lower state triplet separation Eq. (1), the mean fine-structure interval may be determined by [5]

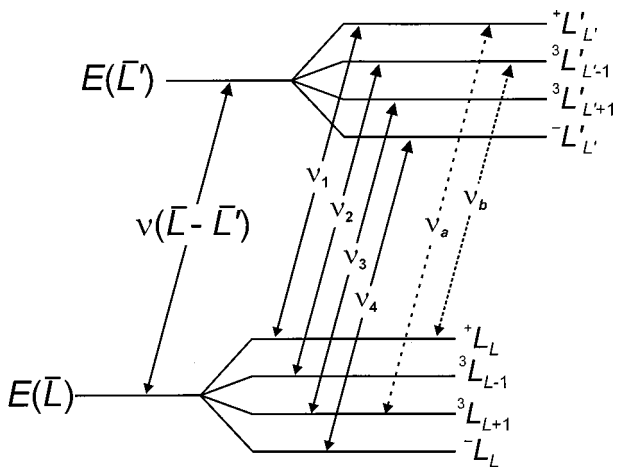

FIG. 3. Generic spin structure level diagram showing the mean interval energy we deduce from measurements. All levels are labeled by ${}^{2S+1}L_J$ with the + and − indicating admixtures of the singlet and triplet $J=L$ states. The four strong transitions are labeled $\nu_1=\nu({}^+L_L-{}^+L'_{L'})$, $\nu_2=\nu({}^3L_{L-1}-{}^3L'_{L'-1})$, $\nu_3=\nu({}^3L_{L+1}-{}^3L'_{L'+1})$, and $\nu_4=\nu({}^-L_L-{}^-L'_{L'})$. Two weak transitions, $\nu_a=\nu({}^3L_{L+1}-{}^+L'_{L'})$ and $\nu_b=\nu({}^+L_L-{}^3L'_{L'-1})$, are also pictured.

$$\nu(\bar{L}-\bar{L}')=\frac{1}{4}\left[\nu_1+\frac{2L'-1}{2L'+1}\nu_2+\frac{2L'+3}{2L'+1}\nu_3+\nu_4\right]-\left[\frac{1}{4L+2}-\frac{1}{4L'+2}\right]\nu({}^3L_{L-1}-{}^3L_{L+1}). \tag{2}$$

Values of our five G-H and H-I mean intervals, along with the individual MFS intervals, are tabulated below in Table II.

IV. EXPERIMENTAL LINE SHAPES AND DATA FITS

We found that our data are best fit with a line shape that includes contributions from cascades from states above those we are examining. These cascade contributions experience a shorter interaction time with the rf field and lead to a broadening of the resonance line. Assuming a two-level system with a constant feed rate and a fraction α of the signal that is due to cascades, and an average (hydrogenic) lifetime of the two states, we expect a line shape of the form

$$S_i(\nu)=(1-\alpha)\frac{\sin^2(\pi b_i T)}{b_i^2}e^{-\gamma T}+\frac{\alpha}{Tb_i^2}\left[\frac{e^{-\gamma T}}{-2\gamma}-\frac{e^{-\gamma T}}{\gamma^2+4\pi^2 b_i^2}\times\left[\frac{-\gamma}{2}\cos(2\pi b_i T)+\pi b_i\sin(2\pi b_i T)\right]+\frac{1}{2\gamma}-\frac{\gamma/2}{\gamma^2+4\pi^2 b_i^2}\right],$$

where

TABLE II. Helium MFS intervals ν_i and mean intervals determined by Eq. (2). This table does not include the systematic effects discussed in Sec. V, except for the ac Stark shift. The $10G$-H values are an average of two data sets.

	$7G$-H	$7H$-I	$9G$-H	$9H$-I	$10G$-H
$\nu(\overline{L}'-\overline{L})$	1359.0026(25)	423.4906(11)	665.85016(52)	211.79253(24)	491.00724(31)
ν_1	1346.9305(49)	416.5355(20)	660.16274(99)	208.52075(44)	486.85946(54)
ν_2	1352.1632(58)	419.8780(23)	662.63637(117)	210.09393(49)	488.66564(68)
ν_3	1361.7808(44)	425.1736(20)	667.16164(87)	212.58242(39)	491.96548(50)
ν_4	1372.2749(49)	431.0602(22)	672.09219(100)	215.35337(44)	495.55674(57)
$\nu({}^3L_{L+1}-{}^3L_{L-1})$	27.523(33)	17.897(32)	12.990(13)	8.466(13)	9.446(15)

$$b_i=[(2V)^2+(\nu-\nu_i)^2]^{1/2},$$

$$V=\frac{eE}{2h}\langle n,l|z|n',l'\rangle,$$

$$\gamma=(1/\tau+l/\tau')/2.$$

The parameter T is the interaction time for atoms that travel the entire length of the rf region. V is the electric dipole matrix element with an rf electric field of amplitude E. The first term in $S_i(\nu)$ is the familiar sinc function that is independent of cascades. We vary α and V in our fits. The parameter α ranges from 0.2 to 0.5, and is generally larger for states with shorter lifetimes.

Another feature included in our fit line shapes is rf reflections due to impedance mismatches at the ends of our rf region. Reflections contribute to our line shape in two ways. First, there is a term that is proportional to the square of the reflection coefficient, Γ^2, and has a Doppler shift in the opposite direction to the primary rf wave. This term is very small and is of negligible importance in our fits. Second, there is a term proportional to Γ that is due to an interference between the forward and backward traveling (reflected) waves. This term is of the form

$$R_i(\nu)=2\,\mathrm{Re}(\Gamma)\,\frac{\sin[\pi(\nu-\nu_i+\delta)T]\sin[\pi(\nu-\nu_i-\delta)T]}{(\nu-\nu_i+\delta)(\nu-\nu_i-\delta)},$$

where ν is the transition frequency and $\delta_i=\beta\nu_i$ is the Doppler shift. Fit values of $\mathrm{Re}\,(\Gamma)$ vary from 0.077(5) at worst (in the $7G$-H measurements) to about 0.003(3) at best for the $n=9$ measurements.

The total fit line shape is the sum of four cascade line shapes and their corresponding reflections with individual amplitudes A_i:

$$S(\nu)=\sum_{i=l}^{4} A_i[S_i(\nu)+R_i(\nu)].$$

The data for both directions of rf propagation were fit with common reflection coefficients $\mathrm{Re}(\Gamma)$, interaction times T, coupling strengths V, cascade parameters α, and a beam velocity βc. The center frequencies of each of the four MFS peaks for stationary atoms (ν_i) were free parameters, with the four Doppler-shifted peak centers determined by

$$\nu_i^{\pm}=\nu_i\times\left(\frac{1\pm\beta}{1\mp\beta}\right)^{1/2}.$$

A fifth weak transition (the $n\ {}^3L_{L+1}-n\ {}^3L'_L$) was included in the fit with a variable amplitude, which was typically a few percent of the allowed transition amplitudes. Its frequency, ν_5 was fixed relative to the first spin component frequency ν_i, by a theoretical frequency offset $\delta=\nu_1-\nu_5$. As an example, for the $9H$-I interval, Drake's value [10] for ν_1 and ν_5 are $\nu_1=208.519\,17$ MHz and $\nu_5=206.076\,63$ MHz, giving $\delta=2.442\,54$ MHz. Our fit is not very sensitive to the value of δ, and varying it by 5% shifts the value of the mean $9H$-I interval by less than $\frac{1}{10}$ of its experimental uncertainty.

Figures 4–6 show some of our data along with theoretical fits. The data in the figures are what we call a ''symmetrically shifted'' average of data. These sets are a combination of four sets of data each, two for each direction of rf propagation and two for each rf region orientation. In order to average these four sets, we first ''shift'' each set by adding an offset to the data's frequency column that is the size of its Doppler shift rounded to the nearest frequency step. For example, for a 9 kV, $7G$-H data set, the Doppler shift between copropagating and counterpropagating sets of data is about 6.0 MHz. To average these sets, we adjust the frequency scale of the copropagating set by -3.0 MHz, and the counter set by $+3.0$ MHz, then average the two together. These sets are then averaged with sets taken with the rf region reversed, and the results may be seen in Fig. 4.

This form of averaging has several benefits. First, we may present all of our data for a given velocity in a single figure, which shows a representative S/N ratio. Second, all of the rf reflection structure in such a figure is symmetric about each peak. A fit of such an averaged set will thus be less sensitive

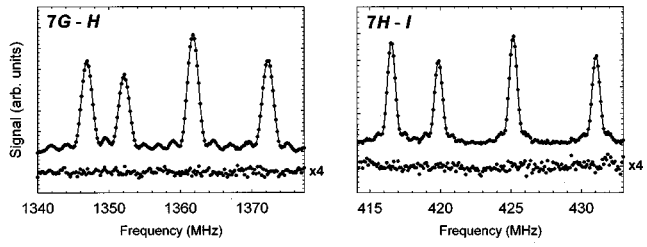

FIG. 4. $n=7$ transitions. The four MFS components in each spectrum are, from left to right, ν_1, ν_2, ν_3, and ν_4. The residuals of the fit are included offset beneath the data, magnified by a factor of 4.

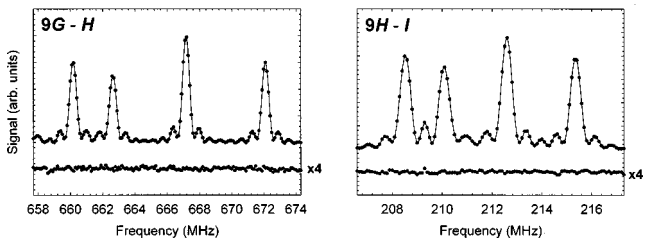

FIG. 5. $n=9$ transitions. The four MFS components in each spectrum are, from left to right; ν_1, ν_2, ν_3, and ν_4. The residuals of the fit are included offset beneath the data, magnified by a factor of 4.

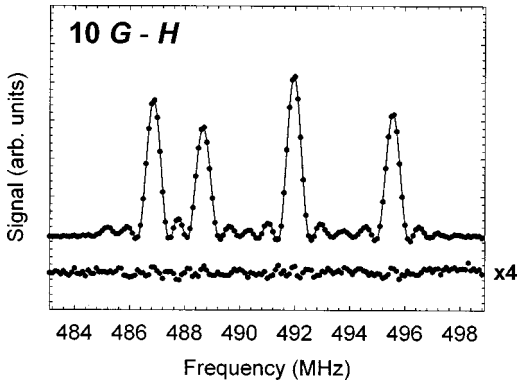

FIG. 6. $n=10$ transitions. The four MFS components in this spectrum are, from left to right, ν_1, ν_2, ν_3, and ν_4. The residuals of the fit are included offset beneath the data, magnified by a factor of 4.

to systematic shifts from these reflections. As long as our step size is reasonably small, the imperfect overlap of the two sets of data simply results in a slight broadening of the features. Fitting to line centers in a symmetrically shifted average of our data yields the center frequencies of each MFS component, without having to adjust for Doppler shifts (the second-order Doppler correction still must be applied.) We fit the symmetrically shifted data sets using symmetric reflections about our line shapes, and found excellent agreement with the primary fits performed keeping each direction of propagation separate, as discussed at the beginning of this section. The results reported in this paper were all determined from the primary fits, but the excellent agreement with the results of the ''symmetric shifted'' method show that our results are not sensitive to the way in which we averaged our multiple data sets.

The extracted fit values for the four allowed MFS transitions for each interval are tabulated in Table II. The lower state triplet separation is also included in the table, and was used with Eq. (2) to determine the mean intervals listed. It is also of interest to compare the differences between the four individual transition frequencies and the mean interval with theoretical predictions. Table III lists the differences between the observed shifts of each MFS component from the mean fine-structure interval [labeled by $\Delta_i=(\nu_i-\overline{\nu})$] and theoretical predictions. For example, for the $7G$-$7H$ interval,

$$\Delta_1=\nu({}^{+}L'_{L'}-{}^{+}L_L)\text{-}\nu(\overline{L'}-\overline{L})=-12.0721(55)\ \text{MHz}.$$

From Table II, we find that for this transition, E-T: $\Delta_1=-12.0721(55)-[-12.070\,43(24)]=-0.0017(55)$. The values in Table III have been corrected for ac Stark Shifts (see Sec. V below for details). Overall, Table III shows agreement with theoretical spin structure at the level of a few hundredths of a percent.

V. SYSTEMATIC EFFECTS

A number of systematic effects must be accounted for in the analysis of our data. These vary substantially in size and importance. Our analysis includes ac and dc Stark Shifts, Bloch-Siegert shifts, blackbody radiation shifts, rf power variations, shifts due to our time-base calibration, and shifts due to our amplification/detection time constant.

Estimates of ac Stark shifts were made using a dressed-state approach. Weakly coupled transitions result in level anticrossings that produce small shifts in the measured transition frequencies. Each spin-component fit frequency was corrected for ac Stark shifts. These shifts were on average 10–20 times smaller than the statistical uncertainty in each mean interval. The same calculations used to determine these ac Stark shifts correctly predicted the shift rates of the weaker transitions ν_a and ν_b (discussed above), which were taken at much higher powers.

The primary systematic difficulty in our measurements was due to dc Stark shifts. Small stray electric fields ($E_{\rm rms}<50\,\text{mV/cm}$) arise from a number of sources: (i) incomplete cancellation of the earth's magnetic field, (ii) charging of nominally conducting surfaces, and (iii) contact potential differences between surfaces of different metals. These fields were kept small as described in Sec. II.

In order to correct for dc Stark shifts due to stray and motional electric fields, we rely on measurements of Stark-shifted highly excited states, which shift much faster than the lower states that we are interested in. Two transitions were used to determine the effective mean fields within our rf region during each measurement. Either the $17\ {}^1F$-${}^1G$ transition or the $20G$-H transition was recorded between data sets (see Table I for a list of the diagnostic transitions used

TABLE III. Frequency offsets of individual MFS transitions relative to mean intervals, $\Delta_i=(\nu_i-\overline{\nu})$, compared with theory [10]. All values are in kHz.

Expt.-Theory [10]	$7G$-H	$7H$-I	$9G$-H	$9H$-I	$10G$-H
E-T: Δ_1	−1.7(55)	−1.6(23)	−1.1(11)	−0.1(5)	−0.8(6)
E-T: Δ_2	8.3(63)	−1.0(25)	1.0(13)	0.6(6)	0.3(8)
E-T: Δ_3	3.6(50)	1.1(22)	−0.6(10)	−1.4(5)	0.3(6)
E-T: Δ_4	−9.8(55)	1.1(24)	−0.9(11)	−0.1(5)	−0.1(6)

TABLE IV. Systematic shifts: Contributions to each mean interval. All values are in kHz.

Systematic	$7\overline{G}\text{-}\overline{H}$	$7\overline{H}\text{-}\overline{I}$	$9\overline{G}\text{-}\overline{H}$	$9\overline{H}\text{-}\overline{I}$	$10\overline{G}\text{-}\overline{H}$ (a)	$10\overline{G}\text{-}\overline{H}$ (b)
Bloch-Siegert	0.20(2)	0.055(6)	0.035(4)	0.110(11)	0.051(5)	0.051(5)
dc Stark	−0.22(4)	0.15(3)	−1.03(20)	−0.90(18)	−1.65(33)	−0.50(10)
BBR	0.21(2)	0.22(2)	0.155(16)	0.173(17)	0.143(14)	0.143(14)
HP time base	0.68(7)	0.21(4)	0.33(7)	0.10(2)	0.25(5)	0.25(5)
Time constant	2.63(27)	1.32(14)	1.32(14)	1.32(14)	1.32(14)	0.0
Power variations	−.3(04)	0.0	0.0	0.0	0.0	0.0

for each interval measurement). The $17\ ^1F\text{-}^1G$ transition has a theoretical line center at $\nu_{\text{theo}}=418.432$ MHz and a Stark-shift rate of $R_{17\ ^1F\text{-}^1G}=-337.4\ \text{MHz/(V/cm)}^2$ (averaged over m). The center frequency is calculated using Drake's quantum defect extrapolation [10]. The $20G\text{-}H$ transition has unresolved structure that ranges from the $20\ ^+G_4\text{-}^+H_5$ at $\nu_{\text{theo}}=63.096$ MHz to the $20\ ^-G_4\text{-}^-H_5$ transition at $\nu_{\text{theo}}=64.183$ MHz. We fit our data for the $20G\text{-}H$ resonances to four cascade line shapes that were separated by theoretical separations, with statistical strengths. These transitions have an average Stark-shift rate of $R_{20G\text{-}H}=-2422.3$ MHz/(V/cm)^2. All Stark-shift rates cited above were determined using the results of second-order perturbation theory [11] averaged assuming a uniform distribution in m, and are assumed to be good to 20%. The diagnostic shift rates (designated by $R_{\text{diagnostic}}$ below) are considerably larger than the shift rates calculated for our measured fine-structure intervals, R_{fs} (given in MHz/(V/cm)^2; $R_{7G\text{-}H}=-0.17$, $R_{7H\text{-}I}=+1.6$, $R_{9G\text{-}H}=-4.8$, $R_{9H\text{-}I}=-4.2$, and $R_{10G\text{-}H}=-12.2$.

As an experimental check of the theoretical Stark-shift rates, we measured the induced Stark shifts in the two diagnostic resonances ($17\ ^1F\text{-}^1G$ and $20G\text{-}H$) for a range of potentials V_{app} applied to the rf region's conductor. These measurements were fit to a quadratic form (see below) in order to extract the Stark-shift rates in a manner similar to that of Hessels *et al.* [5]. In contrast to Hessels' measurements, there is an analytic solution for the dc fields due to an applied potential on the conductor [12] that provides a good estimate of the effective separation parameter d, where F_{app} (V/cm) $=V_{\text{app}}/d$. Using d, we determine the Stark-shift rate R by fitting to the following function:

$$\nu=\nu_0-R(F_{\text{stray}}-F_{\text{app}})^2.$$

Our measurements of $R_{\text{diagnostic}}$ for both diagnostic transitions are in agreement with the above theoretical estimates. The fit values for ν_0 were slightly shifted from the theoretical values ν_{theo} because we cannot completely null out stray fields by simply applying a uniform field in one direction. These values suggest that, at best, this method of reducing fields minimizes the residual fields to about 5 mV/cm rms.

Stark-shift corrections were obtained using the above fine-structure shift rates R_{fs}, the observed resonance frequency ν_{obs}, and the theoretical frequency ν_{theo} [10] by

$$\Delta E_{\text{Stark}}=\frac{R_{\text{fs}}}{R_{\text{diagnostic}}}(\nu_{\text{obs}}-\nu_{\text{theo}}).$$

Corrections obtained from this are listed in Table IV.

The Bloch-Siegert effect contributes a small systematic shift to each interval of $\Delta_{\text{BS}}=V^2/\omega$, where ω is the interval frequency and V is the on-resonance Rabi frequency. Since we are near optimum rf power, V is related to the interaction time T by $VT=\pi/2$. Bloch-Siegert shifts are listed in Table IV for the various transitions measured. We attribute an arbitrary 10% uncertainty to these effects, due to limitations in our knowledge of the rf power in the transmission line.

Thermal, blackbody radiation will shift Rydberg states via a dynamic Stark effect [13]. States separated by energies less than 2.6 times the peak energy of the black body radiation distribution, given by

$$u(\omega,T)=\frac{\hbar}{\pi^2c^3}\frac{\omega^3}{e^{\hbar\omega/kT}-1},$$

will shift together, while states with energy separations larger than 2.6 times the peak in thermal radiation repel each other. In order to calculate the effects of BBR on a given interval, one must calculate the shifts in each state due to neighboring states. The total interval shifts found this way are on the order of 0.1 kHz (see Table IV). An uncertainty of 10% has been included in this value to account for possible uncertainty in the radiation temperature which was taken to be 300 K for all of our measurements except for the $7G\text{-}H$,

TABLE V. Mean intervals and comparison with theory. All intervals are in MHz unless otherwise noted. Also tabulated are the theoretical values for V_{ret} and V''.

	$7\overline{G}\text{-}\overline{H}$	$7\overline{H}\text{-}\overline{I}$	$9\overline{G}\text{-}\overline{H}$	$9\overline{H}\text{-}\overline{I}$	$10\overline{G}\text{-}\overline{H}$
Experiment	1359.0003(25)	423.4887(11)	665.849 35(58)	211.791 73(33)	491.007 22(39)
Theory [10]	1359.0028(3)	423.48887(5)	665.8490(2)	211.7909(1)	491.008 23(6)
$E-T$ (kHz)	−2.5(2.5)	−0.2(11)	0.34(58)	0.86(33)	−1.02(36)
V_{ret} [16] (kHz)	−116.00	−33.59	−57.14	−17.00	−42.20
V'' [6,7] (kHz)	−2.11	−1.35	−0.98	−0.62	−0.71

TABLE VI. Comparison between this work and previous measurements.

	This work	Previous work
$7\overline{G}$-$\overline{H}$	1359.0003(25)	1359.16(11) [14]
$7\overline{H}$-$\overline{I}$	423.4887(11)	402.8(4.7) [14]
$10\overline{G}$-$\overline{H}$	491.007 22(39)	491.002(10) [17]
$10\overline{G}$-$\overline{H}$	491.007 22(39)	491.0090(13) [4]
$10\overline{G}$-$\overline{H}$	491.007 22(39)	491.005 23(49) [5]

in which we heated the region to 363 K. This corresponds to an uncertainty in T of about 4%.

In order to correct for possible variation of the rf field amplitude with frequency, we carefully measured the power leaving the transmission line under the conditions of each experiment. From these measurements, we can infer the forward traveling-wave amplitude versus frequency. This procedure is limited by the reflection coefficient at the output of the transmission line, which leads to a mismatch uncertainty. The shifts due to rf power variations were particularly severe for our $7G$-H measurement, in which we used an rf transmission line with relatively large reflections. In order to model these shifts, we created a theoretical mock-up of our data including saturation effects and rf power that varied according to our measurements. We fit these spectra using the same fit algorithm that we used in our data analysis, and observed what the net shift due to the observed power variations was. Since we were close to optimum rf power, the experimental line shapes were not very dependent on rf power, and the required corrections are considerably smaller than naive estimates. Our $7G$-H interval required a correction of $+0.3(4)$ kHz due to this effect.

Comparison of our HP rf synthesizer's 10 MHz time base with another unit's time base that had been calibrated several months earlier indicated that our time base was in error by 0.5 ppm. The uncertainty in the newly calibrated source was $\sim$0.1 ppm, given a possible calibration drift of 0.1 ppm/year, and thus we chose to correct each of our measured intervals by 0.5(1) ppm.

The last source of systematic error that we found in our experiments came from an effective time constant in our detection circuitry that was longer than the 10-ms time constant of the lock-in amplifier. We took data by scanning from low to high frequency. Any random fluctuations in signal amplitude averaged out in the six scans recorded daily. Waiting 1 sec between data points should have provided enough time for the lock-in signal to stabilize, after which each point was averaged for 5 sec. However, when we directly checked this by scanning down in frequency, we found a surprisingly large effect. In order to measure this systematic effect, we scanned the rf frequency both up and down the second time we measured the $10G$-H interval, alternating between the two directions. Fitting the resulting data separately for each scan direction allowed us to determine the systematic shift due to using a single scan direction [$\Delta = 1.32(14)$ kHz]. Analysis of the effect of such an effective ''time constant'' shows that it is proportional to the frequency step size, and our $7G$-H data had to be corrected for twice the normal correction because they used a 0.2 MHz frequency increment. We repeated the $10G$-H measurement, scanning in both directions to remove the shifts. We found that our results were in complete agreement with the previous time-constant corrected results [$\nu_{10G\text{-}H} = 491.007\,24(49)$ compared with $\nu_{10G\text{-}H} = 491.007\,19(52)$].

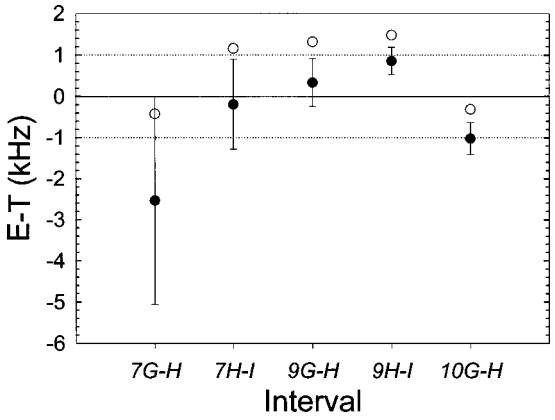

FIG. 7. Differences between the measured (E) and calculated (T) values of the mean fine-structure intervals. The solid points compare directly with the calculation of Drake. The open points compare with theory *including* the V'' correction. The error bars, due to experiment, are the same in both comparisons, and are shown only once. The dashed lines indicate ± 1 kHz, the approximate level of agreement between experiment and theory.

For the second set of $10G$-H measurements, the size of other systematic errors was varied. By applying a potential to the center conductor, we nulled out a large portion of the stray electric field and reduced our dc Stark shifts by a factor of more than 3. Also, while reassembling the rf region after having it gold-plated in order to reduce contact potential induced electric fields, we unintentionally increased the size of the rf reflection coefficient in the region by more than a factor of 2 (from $\Gamma = 0.015$ to 0.036). Good agreement between the second $10G$-H measurement and the previous measurement under such drastically different experimental conditions lends increased confidence in our treatment of these systematic errors.

VI. DISCUSSION OF RESULTS

Table V shows our final values for five G-H and H-I intervals. Previous measurements of several of these intervals are presented along with our data in Table VI. Agreement with the earlier measurements is satisfactory in most cases. Two exceptions are the very early measurement of the $7H$-$7I$ interval [14], which is seen to be in error by 4.4σ, and the most recent prior measurement of the $10G$-H interval [5], which differs from our result by 3.3σ. Table V shows the theoretical values of these five mean fine-structure intervals, as obtained from the tabulations of Drake [10], and compares them with our measurements. Figure 7 illustrates the discrepancies, the largest of which are about 1 kHz, as solid points. Since the total contribution of retardation to these intervals is much larger than this, up to 116 kHz as shown in Table V, this confirms the contribution of retardation to these fine-structure intervals with an average precision of about 1%.

The comparison between the measurements and the re-

vised theory including V'' is shown in Fig. 7 as open points. Although the size of the proposed additional retardation correction, V'', is comparable to the discrepancies between our measurements and Drake's calculation, including V'' fails to improve agreement between theory and experiment. A similar conclusion can be drawn from a recent remeasurement of the $10\ ^{+}F_3 - 10\ ^{+}G_4$ interval in helium [15], which is also in good agreement with Drake's calculation, but not if the predicted -1.2 kHz contribution of V'' is included in the theory. The existing evidence suggests that other effects of the same magnitude as V'' may also be contributing to the fine structure. Still, the degree of agreement between *a priori* theory and experiment is generally very good, and in no case worse than 3σ.

ACKNOWLEDGMENT

This work was supported by the National Science Foundation under Grant No. PHY97-31618.

[1] L. Spruch and E. J. Kelsey, Phys. Rev. A **18**, 845 (1978).
[2] S. R. Lundeen, in *Long-Range Casimir Forces*, edited by Frank S. Levin and David A. Micha (Plenum, New York, 1993).
[3] N. E. Claytor, E. A. Hessels, and S. R. Lundeen, Phys. Rev. A **52**, 165 (1995).
[4] E. A. Hessels, F. J. Deck, P. W. Arcuni, and S. R. Lundeen, Phys. Rev. A **41**, 3663 (1990); **44**, 7855 (1991).
[5] E. A. Hessels, P. W. Arcuni, F. J. Deck, and S. R. Lundeen, Phys. Rev. A **46**, 2622 (1992).
[6] C. K. Au and M. A. Mesa, Phys. Rev. A **41**, 2848 (1990).
[7] C. K. Au and M. A. Mesa, Phys. Rev. A **39**, 2789 (1989).
[8] R. W. Dunford, Ph.D. dissertation, University of Michigan, 1978.
[9] P. L. Jacobson, Ph.D. dissertation, Colorado State University, 1998.
[10] G. W. F. Drake, in *Atomic, Molecular, and Optical Physics Handbook*, edited by G. W. F. Drake (AIP Press, Woodbury, NY, 1996), p. 154.
[11] H. A. Bethe and E. E. Salpeter, *Quantum Mechanics of One- and Two-Electron Atoms* (Plenum, New York, 1977), p. 242.
[12] L. D. Landau, E. M. Lifshitz, and L. P. Pitaevskii, *Electrodynamics of Continuous Media* (Pergamon, Oxford, 1984), p. 15.
[13] J. W. Farley and W. H. Wing, Phys. Rev. A **23**, 2397 (1981).
[14] D. R. Cok and S. R. Lundeen, Phys. Rev. A **23**, 2488 (1981).
[15] C. H. Storey, N. E. Rothery, and E. A. Hessels, Phys. Rev. Lett. **75**, 3249 (1995).
[16] J. F. Babb and L. Spruch, Phys. Rev. A **38**, 13 (1988).
[17] S. L. Palfrey and S. R. Lundeen, Phys. Rev. Lett. **53**, 1141 (1984).